

RESEARCH ARTICLE

10.1002/2016JA023194

Special Section:

Major Results From the MAVEN Mission to Mars

Key Points:

- MAVEN observes narrowband whistler mode waves in the Martian magnetosphere
- The whistler mode waves are generated by cyclotron resonance with anisotropic electrons
- The whistler mode waves could play a role in electron precipitation into the Martian atmosphere

Correspondence to:

Y. Harada,
haraday@ssl.berkeley.edu

Citation:

Harada, Y., et al. (2016), MAVEN observations of electron-induced whistler mode waves in the Martian magnetosphere, *J. Geophys. Res. Space Physics*, 121, 9717–9731, doi:10.1002/2016JA023194.

Received 17 JUL 2016

Accepted 23 SEP 2016

Accepted article online 1 OCT 2016

Published online 19 OCT 2016

MAVEN observations of electron-induced whistler mode waves in the Martian magnetosphere

Y. Harada¹, L. Andersson², C. M. Fowler², D. L. Mitchell¹, J. S. Halekas³, C. Mazelle^{4,5}, J. Espley⁶, G. A. DiBraccio⁶, J. P. McFadden¹, D. A. Brain², S. Xu¹, S. Ruhunusiri³, D. E. Larson¹, R. J. Lillis¹, T. Hara¹, R. Livi¹, and B. M. Jakosky²¹Space Sciences Laboratory, University of California, Berkeley, California, USA, ²Laboratory for Atmospheric and Space Physics, University of Colorado Boulder, Boulder, Colorado, USA, ³Department of Physics and Astronomy, University of Iowa, Iowa City, Iowa, USA, ⁴CNRS, IRAP, Toulouse, France, ⁵IRAP, Université Paul Sabatier, Toulouse, France, ⁶NASA Goddard Space Flight Center, Greenbelt, Maryland, USA

Abstract We report on narrowband electromagnetic waves at frequencies between the local electron cyclotron and lower hybrid frequencies observed by the Mars Atmosphere and Volatile Evolution (MAVEN) spacecraft in the Martian induced magnetosphere. The peaked electric field wave spectra below the electron cyclotron frequency were first observed by Phobos-2 in the Martian magnetosphere, but the lack of magnetic field wave data prevented definitive identification of the wave mode and their generation mechanisms remain unclear. Analysis of electric and magnetic field wave spectra obtained by MAVEN demonstrates that the observed narrowband waves have properties consistent with the whistler mode. Linear growth rates computed from the measured electron velocity distributions suggest that these whistler mode waves can be generated by cyclotron resonance with anisotropic electrons. Large electron anisotropy in the Martian magnetosphere is caused by absorption of parallel electrons by the collisional atmosphere. The narrowband whistler mode waves and anisotropic electrons are observed on both open and closed field lines and have similar spatial distributions in MSO and planetary coordinates. Some of the waves on closed field lines exhibit complex frequency-time structures such as discrete elements of rising tones and two bands above and below half the electron cyclotron frequency. These MAVEN observations indicate that whistler mode waves driven by anisotropic electrons, which are commonly observed in intrinsic magnetospheres and at unmagnetized airless bodies, are also present at Mars. The wave-induced electron precipitation into the Martian atmosphere should be evaluated in future studies.

1. Introduction

The conductive ionosphere and mass loading on the Martian atmosphere provide an effective obstacle to the supersonic solar wind flow, forming the bow shock and induced magnetosphere [e.g., Nagy *et al.*, 2004]. Recent observations have revealed a number of transient and temporal processes operating in the Martian induced magnetosphere, suggesting that the Martian magnetosphere is highly dynamic [DiBraccio *et al.*, 2015; Halekas *et al.*, 2015; Harada *et al.*, 2016]. A wide variety of plasma waves and disturbances have been observed in the dynamic Mars-solar wind interaction extending from the ionosphere out to the foreshock region upstream of the bow shock, including electron plasma oscillations in the electron foreshock [Grard *et al.*, 1989; Trotignon *et al.*, 1991, 2000], ion acoustic waves and whistler mode emissions associated with the bow shock [Trotignon *et al.*, 1991], upstream 1 Hz waves [Brain *et al.*, 2002], upstream and magnetospheric ULF waves [Russell *et al.*, 1990; Delva and Dubinin, 1998; Espley *et al.*, 2004; Mazelle *et al.*, 2004; Wei and Russell, 2006; Lundin *et al.*, 2011; Romanelli *et al.*, 2013; Ruhunusiri *et al.*, 2015, 2016a; Dubinin and Fraenz, 2016], Kelvin-Helmholtz vortices at the magnetosheath-ionosphere interface [Ruhunusiri *et al.*, 2016b], and large-amplitude oscillations of plasma density and magnetic fields in the magnetosphere and ionosphere [Gurnett *et al.*, 2010; Halekas *et al.*, 2011]. It is proposed that particle energization by wave-particle interaction contributes significantly to ion escape from the planet [Ergun *et al.*, 2006; Lundin *et al.*, 2011; Lundin, 2011; Dubinin *et al.*, 2012].

Electromagnetic whistler mode waves with frequencies at a fraction of the electron cyclotron frequency are commonly observed in intrinsic magnetospheres [Burtis and Helliwell, 1969; Menietti *et al.*, 2012] and at airless bodies [Santolik *et al.*, 2011; Halekas *et al.*, 2012]. Free energy sources for the whistler mode emissions can be

provided by anisotropic electrons with $T_{e\perp} > T_{e\parallel}$, where $T_{e\perp}$ and $T_{e\parallel}$ are the electron temperatures perpendicular and parallel to the magnetic field, respectively. Large electron anisotropy can be caused by injection of hot plasma into the inner magnetosphere [Anderson and Maeda, 1977; Horne et al., 2003; Li et al., 2008] and by surface absorption of a significant portion of parallel electrons at airless bodies [Santolik et al., 2011; Halekas et al., 2012; Harada et al., 2014]. In particular, the whistler mode chorus waves in the Earth's magnetosphere have been extensively studied because they can play an important role in diffuse auroral precipitation [e.g., Ni et al., 2011] and acceleration of radiation belt electrons [e.g., Horne and Thorne, 2003]. Compared to the numerous observations of the electron-induced whistler mode waves at magnetized planets and airless bodies, there have been only a few reports on such waves in the Martian induced magnetosphere. Grard et al. [1989, 1991] presented Phobos-2 observations of electric field wave spectra which peaked below the local electron cyclotron frequency within the Martian magnetosphere. They postulated these waves as whistler mode emissions based on their frequencies, but this interpretation could not be proven owing to the lack of magnetic field data at the corresponding frequencies. The generation mechanisms and free energy sources for these waves remain unclear. At Venus, impulsive fluctuations of electric and magnetic fields at similar frequencies are observed in the ionosphere, and they are interpreted as lightning-induced electromagnetic waves propagating in the whistler mode [Russell, 1991; Russell et al., 2007, 2008].

This paper presents observations of electric and magnetic field waves with narrowband features at frequencies of $f_{\text{LHR}} < f < f_{\text{ce}}$, where f_{LHR} and f_{ce} are the local lower hybrid and electron cyclotron frequencies, obtained in the Martian induced magnetosphere by the Mars Atmosphere and Volatile Evolution (MAVEN) mission [Jakosky et al., 2015]. We use passive (natural) electric field wave spectra, waveforms, and electron densities obtained by the Langmuir Probe and Waves (LPW) instrument [Andersson et al., 2015], electron data from the Solar Wind Electron Analyzer (SWEA) [Mitchell et al., 2016], magnetic field data from the Magnetometer (MAG) [Connerney et al., 2015], and ion data from the SupraThermal and Thermal Ion Composition (STATIC) [McFadden et al., 2015] on board the MAVEN spacecraft. The MAVEN data demonstrate that the observed waves are consistent with electromagnetic whistler mode waves generated by cyclotron resonance with anisotropic electrons in the Martian magnetosphere. The rest of the paper is structured as follows: Section 2 presents detailed case studies of the narrowband waves and associated electron signatures. Section 3 provides statistical results on spatial distributions of the narrowband waves and anisotropic electrons in the Martian magnetosphere. In section 4, we discuss the observed properties of the narrowband waves and electron anisotropy. Section 5 summarizes the principal conclusions of the paper.

2. Case Studies

2.1. Narrowband Electromagnetic Waves at $f_{\text{LHR}} < f < f_{\text{ce}}$

Figure 1 displays an example of narrowband waves at $f_{\text{LHR}} < f < f_{\text{ce}}$ observed by MAVEN in the Martian induced magnetosphere. MAVEN was traveling over the southern terminator from Mars Solar Orbital (MSO) coordinates of $[0.1, 0.5, -1.1] R_M$ to $[-0.1, 0.3, -1.1] R_M$ at 450–700 km altitudes and 85° – 93° solar zenith angles below the magnetic pileup boundary (MPB). During this time interval, MAVEN observed weak ambient magnetic fields as low as ~ 3.85 nT (corresponding to the minimum $f_{\text{ce}} \sim 108$ Hz as shown by the upper white line in Figure 1a). The electric field wave spectra (Figure 1a) exhibit narrowband features with frequencies of ~ 4 – 20 Hz at 21:26:34–21:27:38 UT (indicated by the dashed oval). We observe peak wave frequencies lower than 16 Hz except around the end of the event. The lowered frequencies of the narrowband electric field waves in the weak magnetic field condition enable examination of their magnetic field counterparts with MAG, which measures magnetic fields with 32 vector samples per second. When the frequency of the narrowband electric field waves falls below 16 Hz, we observe the corresponding magnetic field power in the transverse wave spectra (Figure 1b). Waveform analysis of the magnetic field components [Means, 1972] reveals that these waves have (i) a predominantly transverse component compared to compressional component (Figures 1b and 1c), (ii) a high coherency (yellow to red in Figure 1d), (iii) a quasi-parallel propagation along the background magnetic field (blue in Figure 1e), and (iv) a right-handed polarization (red in Figure 1f). These wave properties and the presence of magnetic field component at $f_{\text{LHR}} < f < f_{\text{ce}}$ are consistent with the whistler mode.

2.2. Narrowband Waves on Open Magnetic Field Lines

Based on the analysis in section 2.1, we can reasonably assume that narrowband waves at $f_{\text{LHR}} < f < f_{\text{ce}}$ with similar spectral features would also be whistler mode waves, although their magnetic field spectra are not always available. Whistler mode waves in this frequency range can be excited by cyclotron resonance with

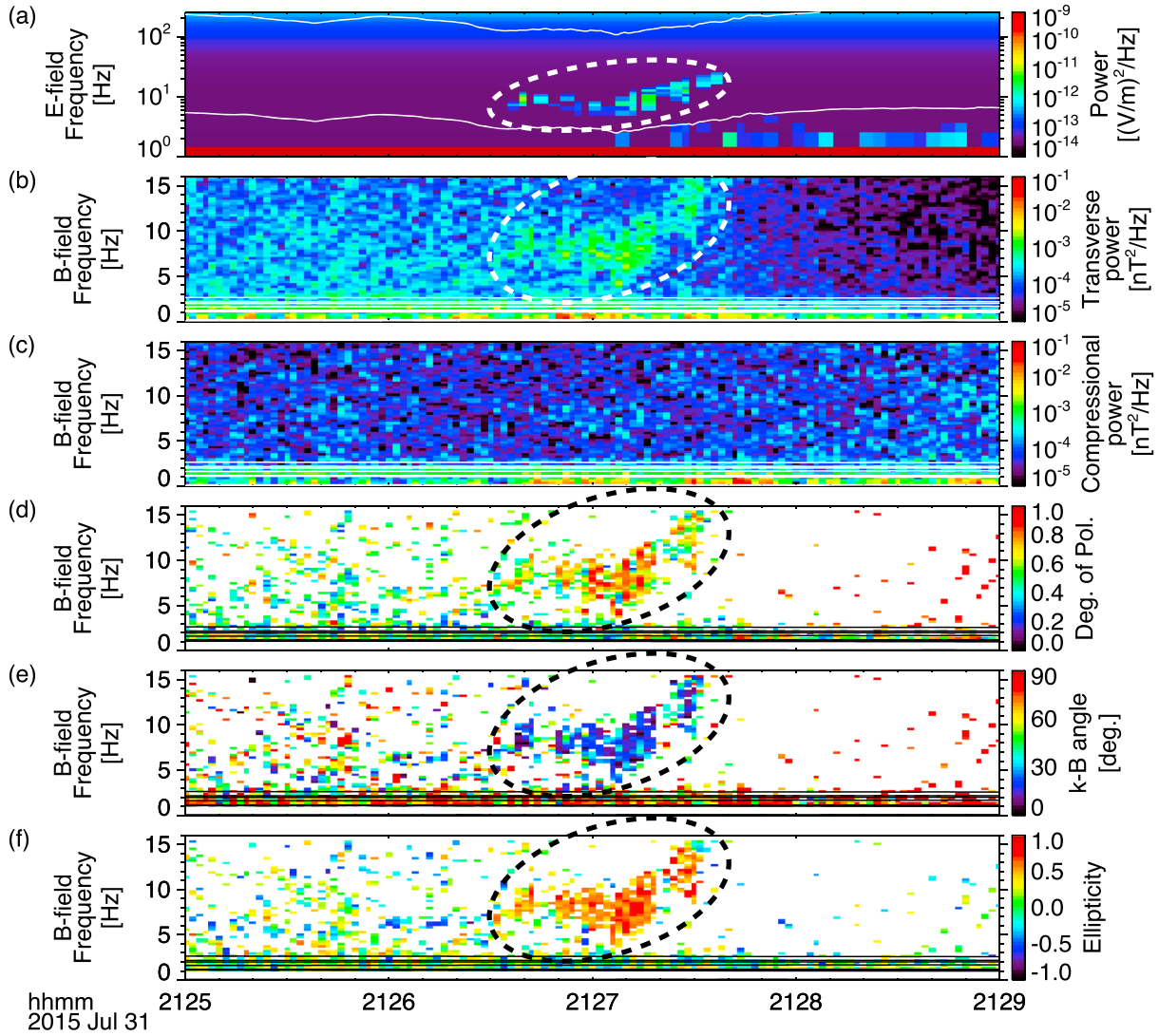


Figure 1. MAVEN observations of (a) electric field wave spectra, magnetic field spectra of (b) transverse and (c) compressional waves, (d) degree of polarization, (e) wave normal angle with respect to the background magnetic field, and (f) ellipticity (positive signs refer to right-handed polarization) at 21:25–21:29 UT on 31 July 2015. Values at each frequency in Figures 1d–1f are shown only if the total spectral intensity exceeds 4×10^{-4} nT²/Hz. The upper and lower white lines in Figure 1a indicate the local electron cyclotron and lower hybrid frequencies. The white and black lines in Figures 1b–1f show the operation frequencies of the four Reaction Wheel Assemblies, which cause the semiconstant artificial tones. The dashed ovals denote the narrowband electromagnetic waves identified as whistler mode waves (see text for detail).

anisotropic electrons ($T_{e\perp} > T_{e\parallel}$). The whistler mode linear growth rate γ as a function of resonant velocity v_{\parallel} and frequency f [Kennel and Petschek, 1966] is

$$\frac{\gamma(v_{\parallel})}{f_{ce}} = \pi \left(1 - \frac{f}{f_{ce}}\right)^2 \eta(v_{\parallel}) \left[A(v_{\parallel}) - \frac{1}{f_{ce}/f - 1}\right], \quad (1)$$

where the fraction of resonant electrons $\eta(v_{\parallel})$ in the total electron density N_e is

$$\eta(v_{\parallel}) = v_{\parallel} F_e(v_{\parallel}) / N_e, \quad (2)$$

the electron-reduced distribution function $F_e(v_{\parallel})$ is

$$F_e(v_{\parallel}) = 2\pi \int f_e(v_{\parallel}, v_{\perp}) v_{\perp} dv_{\perp}, \quad (3)$$

and the electron anisotropy $A(v_{||})$ is

$$A(v_{||}) = \frac{\int \left(v_{||} \frac{\partial f_e}{\partial v_{\perp}} - v_{\perp} \frac{\partial f_e}{\partial v_{||}} \right) \frac{v_{\perp}^2}{v_{||}} dv_{\perp}}{2 \int f_e v_{\perp} dv_{\perp}}, \quad (4)$$

(note that f_e stands for the electron velocity distribution function $f_e(v_{||}, v_{\perp})$). The resonant velocity $v_{||}$ for frequency f is

$$\frac{v_{||}}{V_{Ae}} = \frac{(1 - f/f_{ce})^{3/2}}{(f/f_{ce})^{1/2}}, \quad (5)$$

where $V_{Ae} = B/\sqrt{\mu_0 m_e N_e}$ is the electron Alfvén velocity, B is the magnetic field strength, μ_0 is the vacuum permeability, and m_e is the electron mass.

Here we analyze electron velocity distributions measured by SWEA and investigate whether anisotropic electrons can generate the observed narrowband waves in the Martian magnetosphere. Figure 2 shows another narrowband wave event as well as electron, ion, and magnetic field data obtained by MAVEN in Mars's optical shadow. We find typical signatures of plasma and fields in the Martian magnetotail lobes: cold planetary ions (Figure 2a), hot electrons of sheath origin (Figure 2b, we note that cold planetary electrons may not have been detected by SWEA owing to negative spacecraft charging in shadow and SWEA's lowest measurable energy of 3 eV), and smooth, B_x -dominant magnetic fields (Figure 2f). The 100–1000 eV electron pitch angle distributions (Figure 2c) show signatures of counterstreaming electrons at $\sim 19:40$ – $19:41$ UT and $\sim 19:45$ – $19:46$ UT, indicating that hot electrons of solar wind origin enter the magnetotail along detached field lines with both ends unconnected to the collisional atmosphere. The counterstreaming distributions could originate from the upstream solar wind [e.g., Gosling *et al.*, 2005] or be formed by processes operating in the magnetosheath/magnetosphere. At $\sim 19:42:00$ – $19:44:30$ UT, we observe the narrowband electric field waves at $f \sim 50$ – 100 Hz in the $f_{LHR} < f < f_{ce}$ range (Figure 2e) coinciding with one-sided loss cones on the parallel side (pitch angles $< 90^\circ$ in Figure 2c). This type of electron pitch angle distribution indicates an open magnetic field line configuration with one end of the field line connected to the collisional atmosphere and the other to interplanetary space [Brain *et al.*, 2007; Lillis *et al.*, 2008]. The substantial loss of hot, parallel electrons results in effective temperature anisotropy that can drive whistler mode wave growth as observed at other unmagnetized bodies [Santolik *et al.*, 2011; Halekas *et al.*, 2012; Harada and Halekas, 2016].

We utilize SWEA's Pitch Angle Distribution (PAD) data, which contain electron flux as a function of time, energy, and pitch angle at relatively high time cadence. Assuming that electrons are gyrotropic, this data set can be sorted into electron distributions in $v_{||}$ – v_{\perp} space. Figure 3a shows an example of the electron distribution function, $f_e(v_{||}, v_{\perp})$, at 19:42:46–19:42:47 UT (indicated by the vertical dashed line in Figure 2) corrected for the negative spacecraft potential estimated from the low-energy cutoff of the ion energy spectra (Figure 2a) [Harada *et al.*, 2015a]. From this distribution with the help of electron density information derived from the total ion density measured by STATIC (the corresponding electron plasma frequency is shown by the white dotted line in Figure 2e, which agrees well with the plasma line in the wave spectra), we compute the reduced distribution function, electron anisotropy, and temporal growth rates of whistler mode waves at various resonant velocities (Figures 3b–3d) using equations (1)–(4) in the same manner as Harada *et al.* [2014, 2015b]. The loss of hot, parallel electrons is evident on the $v_{||} > 0$ side of $f_e(v_{||}, v_{\perp})$ and $F_e(v_{||})$ (Figures 3a and 3b), causing large $A(v_{||})$ (Figure 3c). The shape of the resulting $\gamma(v_{||})/f_{ce}$ on the $v_{||} > 0$ side (Figure 3d) is consistent with the observed peak in the electric field wave spectrum (Figure 3e, converted into the $v_{||}$ scheme using equation (5)), suggesting a strong connection between the anisotropic electrons and narrowband waves.

We repeat the growth rate computation for each snapshot of PAD data except for those with poor pitch angle coverage; we discard PAD snapshots if the minimum (maximum) pitch angle of center directions of unblocked solid angle bins is greater (less) than 30° (150°). Figure 2d shows convective growth rates [Summers *et al.*, 2009; Li *et al.*, 2013] in units of dB/ R_M computed by $20/(\ln 10) \cdot 2\pi\gamma \cdot R_M/V_g$, where γ is the temporal linear growth rate in Hz, R_M is the Mars radius in km, and V_g is the wave group velocity in km/s. We observe the peak convective growth rates exceeding 20 dB/ R_M , indicating whistler mode waves can grow substantially within a reasonable spatial scale in the Martian magnetosphere. The peak frequencies of the measured narrowband waves (Figure 2e) are in general agreement with those of the growth rates (the white diamonds in Figure 2e). The agreement of peak frequencies of growth rates and spectral intensities suggests that these waves must have

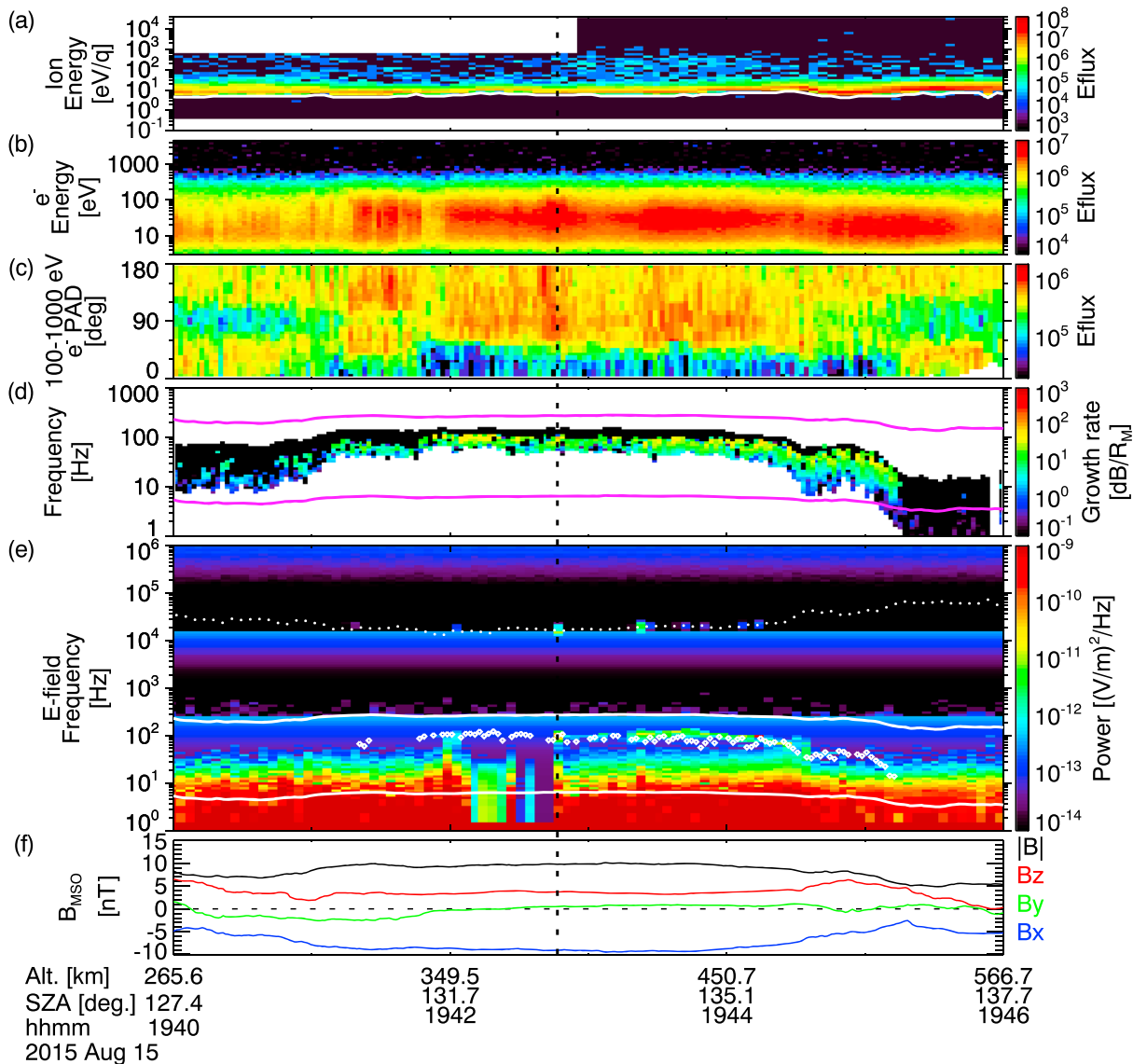


Figure 2. MAVEN observations of (a) omnidirectional ion energy spectra (all species), (b) omnidirectional electron energy spectra, and (c) pitch angle distributions of 100–1000 eV electrons in units of differential energy flux (Eflux) [eV/cm²/s/st/eV], (d) whistler mode convective growth rates computed from the electron velocity distributions (see text for detail), (e) electric field wave spectra, (f) magnetic field in MSO at 19:40–19:46 UT on 15 August 2015. The white line in Figure 2a represents the cutoff energies of the ion energy spectra, which are used to estimate the negative spacecraft potentials. The white dotted line in Figure 2e shows the electron plasma frequency derived from the total ion density. The upper and lower solid lines in Figures 2d and 2e indicate the local electron cyclotron and lower hybrid frequencies. The small white diamonds in Figure 2e represent the peak frequencies of the computed convective growth rates (Figure 2d) for peak rates >20 dB/R_M. The vertical dashed line shows the time of the snapshot shown in Figure 3.

experienced little variation in background plasma and magnetic field conditions as they grow and propagate; i.e., the narrowband whistler mode waves are locally generated by anisotropic electrons.

2.3. Narrowband Waves on Closed Magnetic Field Lines

Narrowband waves are also observed on closed magnetic field lines. Figure 4 shows MAVEN observations of particles and fields on 12 July 2015. During the sunlit interval after 05:59 UT, MAVEN observed cold planetary ions (Figure 4a) and a mixture of ionospheric photoelectrons and hot electrons of solar wind origin (Figure 4b) in moderately strong magnetic fields (Figure 4f). At ~06:00:30–06:04:00 UT, we observe the strong electric field wave emission at $f \sim 30\text{--}500$ Hz in $f_{\text{LHR}} < f < f_{\text{ce}}$ (Figure 4e) accompanied by the enhanced hot electron flux (Figure 4b) with two-sided loss cones (Figure 4c). The flux depletion at both parallel and antiparallel directions is associated with trapped populations on closed field lines with both ends connected to the collisional

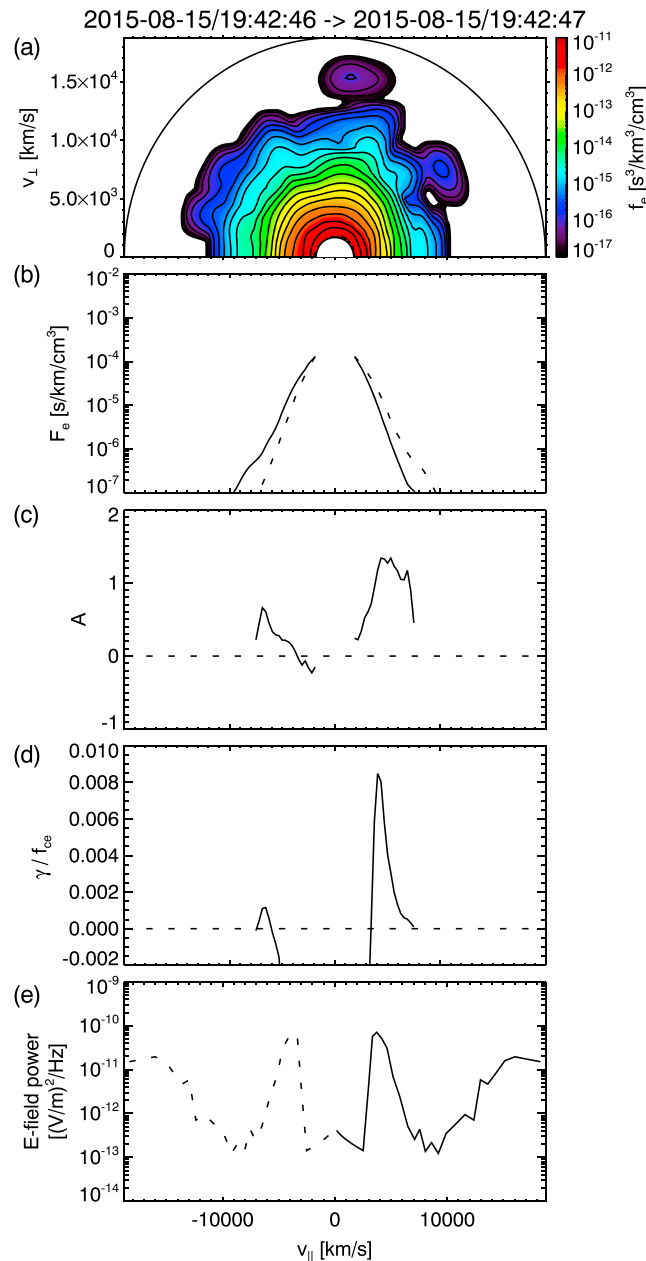


Figure 3. Snapshot at 19:42:46–19:42:47 UT on 15 August 2015 (indicated by the vertical dashed line in Figure 2) of (a) electron velocity distribution function $f_e(v_{\parallel}, v_{\perp})$, (b) reduced distribution function $F_e(v_{\parallel})$, (c) pitch angle anisotropy $A(v_{\parallel})$, (d) whistler growth rate $\gamma(v_{\parallel})/f_{ce}$, and (e) spectral intensity of electric field waves as a function of resonant parallel (solid line) and antiparallel (dashed) velocity for whistler mode waves. The dashed curve in Figure 3b shows v_{\parallel} -flipped distribution $F_e(-v_{\parallel})$ for reference. The $A(v_{\parallel})$ and $\gamma(v_{\parallel})$ are computed only in the v_{\parallel} range where $F_e(v_{\parallel}) > 10^{-7}$ s/km/cm³ to avoid effects of poor counting statistics.

growth rates show rapid wave growth as high as > 100 dB/ R_M (Figure 4d), suggesting that whistler mode waves can grow significantly even within a short traveling distance.

In this event, LPW burst waveform data are available and we can examine microstructures of frequency-time spectrograms. Figure 6 presents four examples of burst waveform segments and their wave spectra processed on ground. The dynamic spectra shown in Figures 6a, 6b, and 6d exhibit discrete elements of rising tones.

atmosphere [Brain et al., 2007; Harada et al., 2016]. This shape of pitch angle distributions also gives rise to large electron anisotropy that can excite whistler mode waves.

We conduct the growth rate computation in the same manner as section 2.2, except that we use electron densities derived from LPW active wave spectra [Andersson et al., 2015] (the corresponding electron plasma frequency is indicated by the white dotted line in Figure 4e). We also assume a zero spacecraft potential in this particular case for the following reasons: The spacecraft was illuminated by sunlight during this time interval, and SWEA did not measure the spacecraft photoelectrons. This indicates that the spacecraft potential, if positive, is lower than the SWEA energy limit of 3 eV. Also, the ion energy spectra (Figure 4a) exhibit cutoff energies < 2 eV, implying spacecraft potentials > -2 V. Using the lower and upper limits of -2 V and $+3$ V, we tested the spacecraft potential effects on the growth rate computation, resulting in no significant difference.

A snapshot again indicates that the loss of hot, parallel (and antiparallel) electrons (Figure 5a) causes large anisotropy (Figure 5c) and rapid wave growth (Figure 5d). Note that this trapped electron distribution is nearly v_{\parallel} symmetric, and both parallel and antiparallel electrons can contribute to the growth of whistler mode waves propagating in the opposite directions, highlighting a clear contrast to the one-sided loss cone shown in Figure 3. The peak of the computed growth rate (Figure 5d) coincides with the wave intensity peak (Figure 5e). Besides, the time series of peak frequencies of growth rates and narrow-band waves display good agreement (the white diamonds and dynamic spectra in Figure 4e). The convective

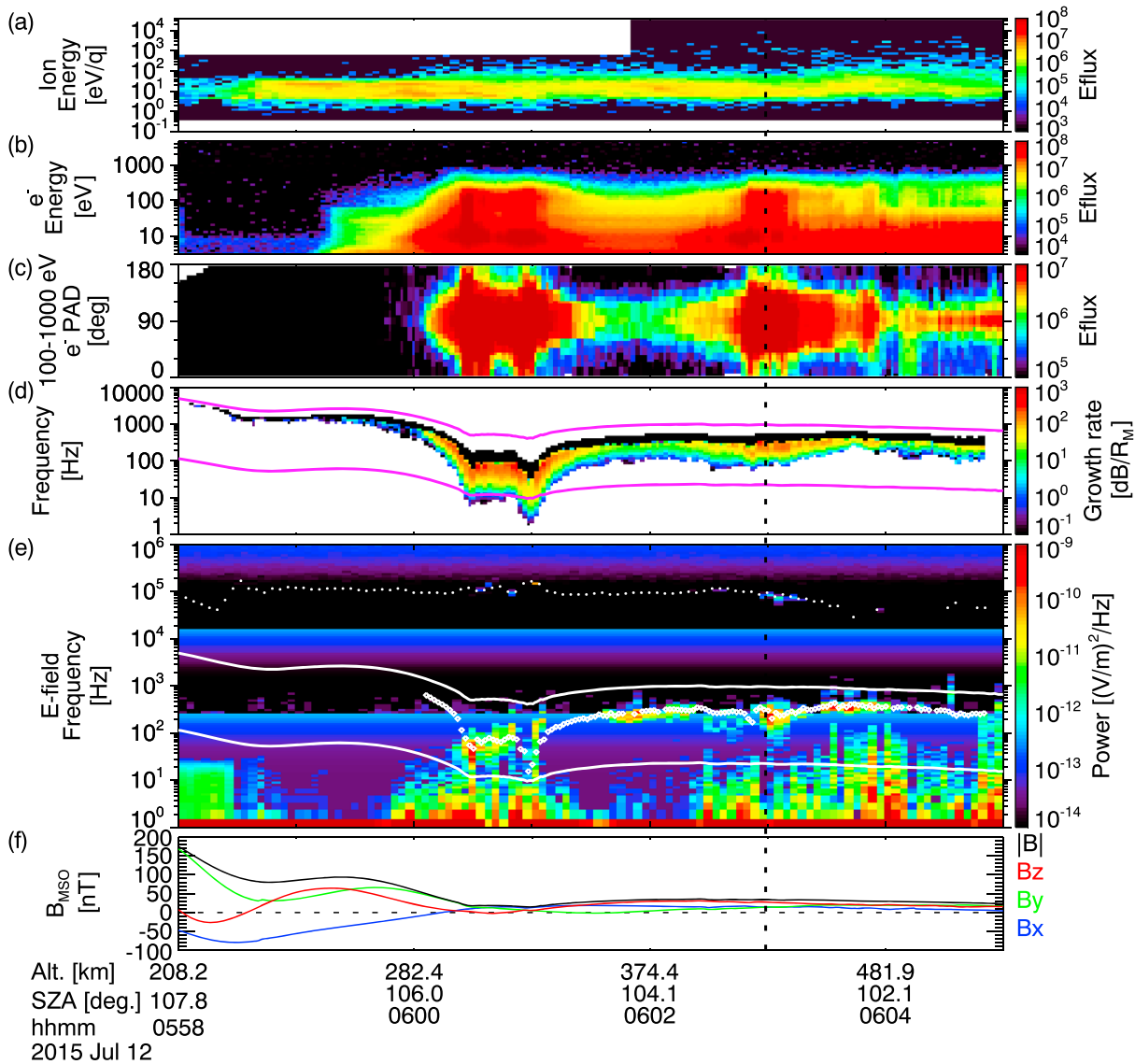


Figure 4. MAVEN observations at 05:58–06:05 UT on 12 July 2015 in the same format as Figure 2, except that the white dotted line in Figure 4e shows the electron plasma frequency obtained from LPW active wave spectra [Andersson et al., 2015].

Figure 6c displays a two-banded structure with a gap around half the electron cyclotron frequency. We point out that these characteristics are strikingly similar to those of the whistler mode chorus observed in the Earth’s magnetosphere [Burtis and Helliwell, 1969, 1976; Tsurutani and Smith, 1974].

3. Statistical Distributions

In this section, we present statistical distributions of the narrowband wave events and anisotropic electrons. We utilize 10 months of MAVEN data obtained from February 2015 to December 2015, during which the LPW L2 merged passive spectra [Andersson et al., 2015] are nearly continuously available. We exclude data obtained outside the nominal magnetic pileup boundary [Trotignon et al., 2006], thereby focusing on waves in the magnetosphere. We also discard wave spectra if one of the electron densities derived from active wave spectra and from current-voltage measurements [Andersson et al., 2015] exceeds 10^4 cm^{-3} , when the electron plasma frequency approaches or exceeds the upper limit of the instrument measurement range and aliasing/contamination occurs at lower frequencies. Based on the remaining “clean” magnetospheric wave spectra, we utilize an automated procedure to identify narrowband wave events with peak frequencies in the $f_{\text{LHR}} < f < f_{\text{ce}}$ band. We first redivide the L2 merged spectra into low-frequency ($<256 \text{ Hz}$) and

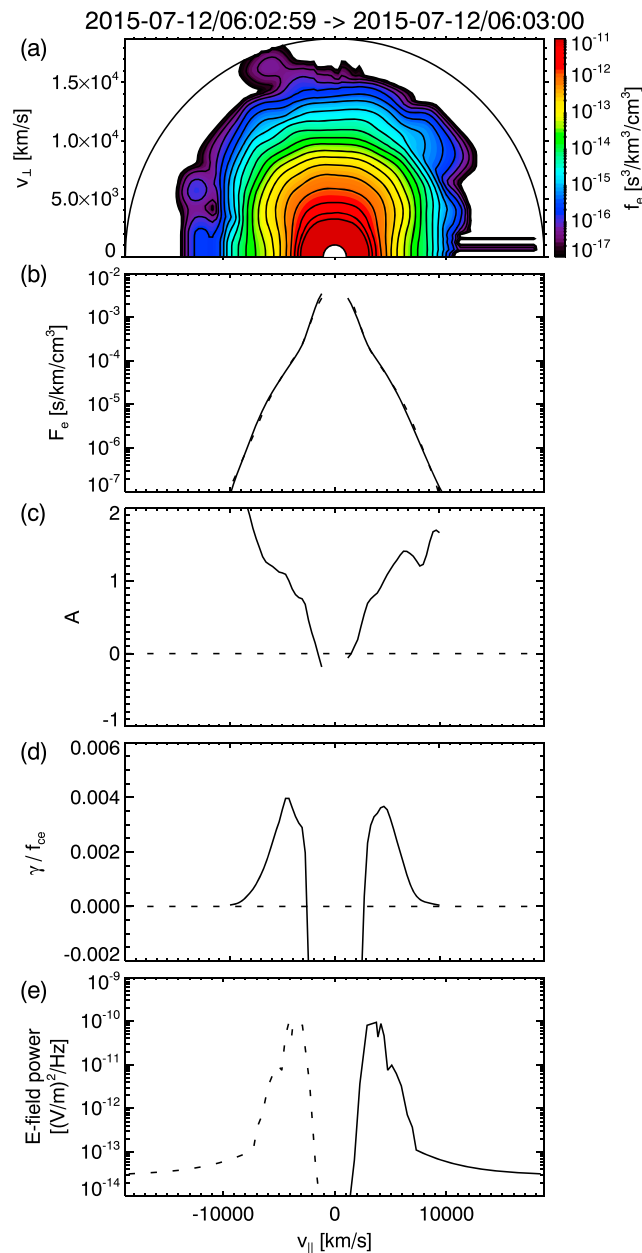


Figure 5. Snapshot at 06:02:59–06:03:00 UT on 12 July 2015 (indicated by the vertical dashed line in Figure 4) in the same format as Figure 3.

altitudes and the spacecraft spent different total times in different regions, the data density is not uniform in the covered area (the gray area in Figure 7a). Therefore, we derive occurrence percentage of the events with variable bin sizes in spherical coordinates as shown in Figure 7b. These distributions show a nonuniform distribution of the narrowband wave events. We find two clusters of events in the cylindrical MSO coordinates: (i) the dayside events distributed just below the nominal MPB and (ii) the nightside events distributed broadly in the near-Mars magnetosphere mainly at a distance from the center of Mars $R < 2 R_M$.

Next we present spatial distributions of anisotropic electrons based on SWEA PAD data obtained in the same interval. First, we conduct spacecraft potential correction. When the spacecraft is located in shadow or at low altitudes < 250 km, where generally negative potentials are expected, we use negative spacecraft potentials derived from the low-energy cutoff of ion energy spectra. At sunlit high altitudes, where positive potentials are usually observed, we use positive spacecraft potentials estimated from the edge of spacecraft photoelectrons

medium-frequency (256 Hz–16 kHz) subsets to avoid effects of artificial discontinuities in the merged spectra. We then smooth each of the low- and medium-frequency subsets over frequency with a width of three frequency steps so that small noisy features in spectra will not be accidentally taken as peaks. From these smoothed spectra, we search spectral intensity peaks at $f_{LHR} < f < f_{ce}$ with over an order of magnitude increase compared to the minimal intensity in the $f/2 < f < 2f$ band. We also require the peak intensity to be in the 10^{-12} – 10^{-8} (V/m)²/Hz range to eliminate extremely weak peaks and unusually strong peaks, the latter of which could be nongeophysical noise. As seen later, most of the naturally occurring wave peaks are below $\sim 10^{-9}$ (V/m)²/Hz. Once we obtain the narrow intensity peaks for time series of spectra, we select persistent peaks lasting for at least two consecutive time steps with peak frequency change rates smaller than a factor of 4 per time step. In this way, random peaks seen in turbulent fluctuations are mostly filtered out. Out of 826,254 valid spectra obtained in the magnetosphere, we found 1179 individual narrowband wave events (which can be grouped into 459 segments of consecutive events).

Figure 7a shows the narrowband wave event distribution in cylindrical MSO coordinates (as a function of X_{MSO} and ρ_{MSO} , where $\rho_{MSO} = \sqrt{Y_{MSO}^2 + Z_{MSO}^2}$) with colors indicating peak intensities. The vast majority of the identified events have peak intensities between 10^{-12} and 10^{-10} (V/m)²/Hz. Since the LPW time cadence varies at different

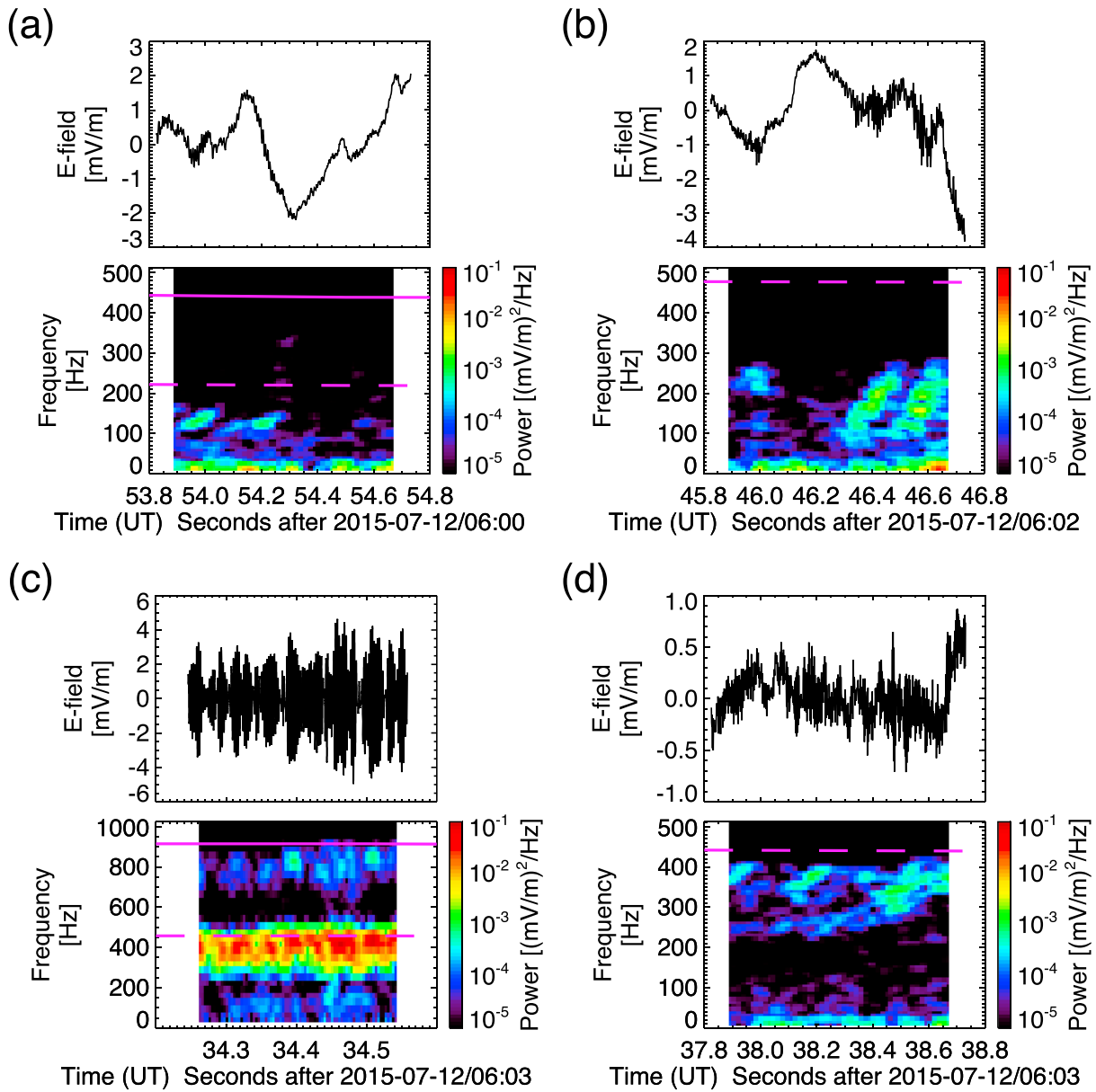


Figure 6. LPW burst waveform data and ground-processed wave spectra at (a) 06:00:53.8–06:00:54.8 UT, (b) 06:02:45.8–06:02:46.8 UT, (c) 06:03:34.2–06:03:34.6 UT, and (d) 06:03:37.8–06:03:38.8 UT on 12 July 2015. The magenta solid and dashed lines indicate the local f_{ce} and $f_{ce}/2$, respectively.

in electron energy spectra. Once each velocity distribution is corrected for spacecraft potentials in units of distribution function, the electron anisotropy, $A(v_{||})$, is computed as described in section 2.2. Then $A(v_{||})$ is averaged in the 4000 km/s $< |v_{||}| < 10,000$ km/s range (parallel energies of 45–284 eV). This $|v_{||}|$ range is chosen so that it includes typical parallel velocities of unstable electrons relevant to the narrowband waves at $f_{LHR} < f < f_{ce}$ (cf. Figures 3 and 5) yet the uncertainty of the estimated spacecraft potentials has minimal effects on the computed quantities.

Figure 7c shows the $X_{MSO} - \rho_{MSO}$ distribution of medians of the electron anisotropy. The anisotropic electrons show very similar distributions to the narrowband wave events. We observe the anisotropy enhancement (i) near the dayside MPB and (ii) in the nightside near-Mars magnetosphere. The general agreement of the spatial distributions suggests that the anisotropic electrons provide a free energy source for the narrowband whistler mode waves observed in the Martian magnetosphere.

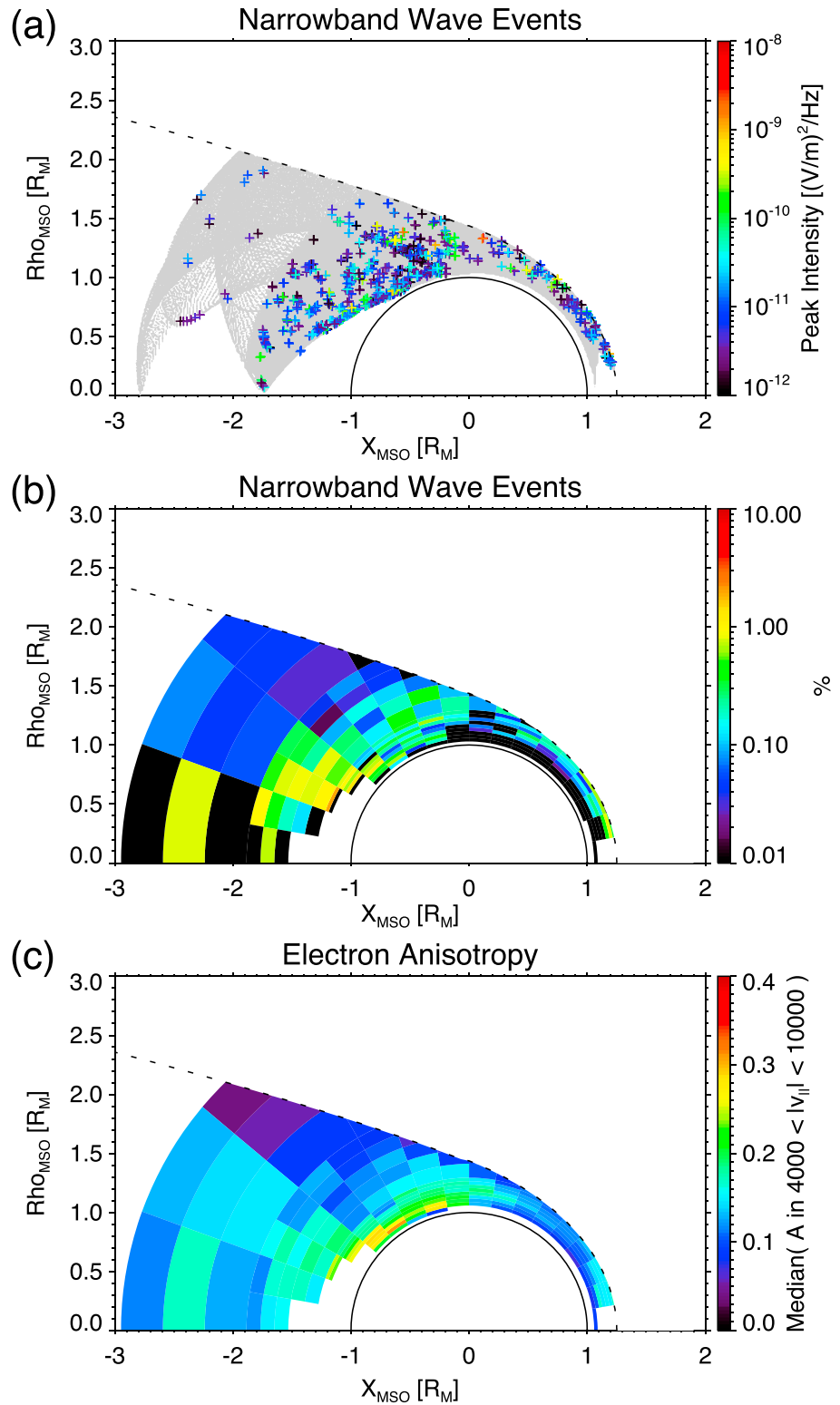


Figure 7. Cylindrical MSO distributions of (a) narrowband wave events, (b) percentage of event occurrence, and (c) medians of electron anisotropy averaged in the 4000 km/s < $|v_{||}|$ < 10,000 km/s range. The Sun direction is to the right. The dashed lines indicate the nominal position of the magnetic pileup boundary [Trotignon et al., 2006].

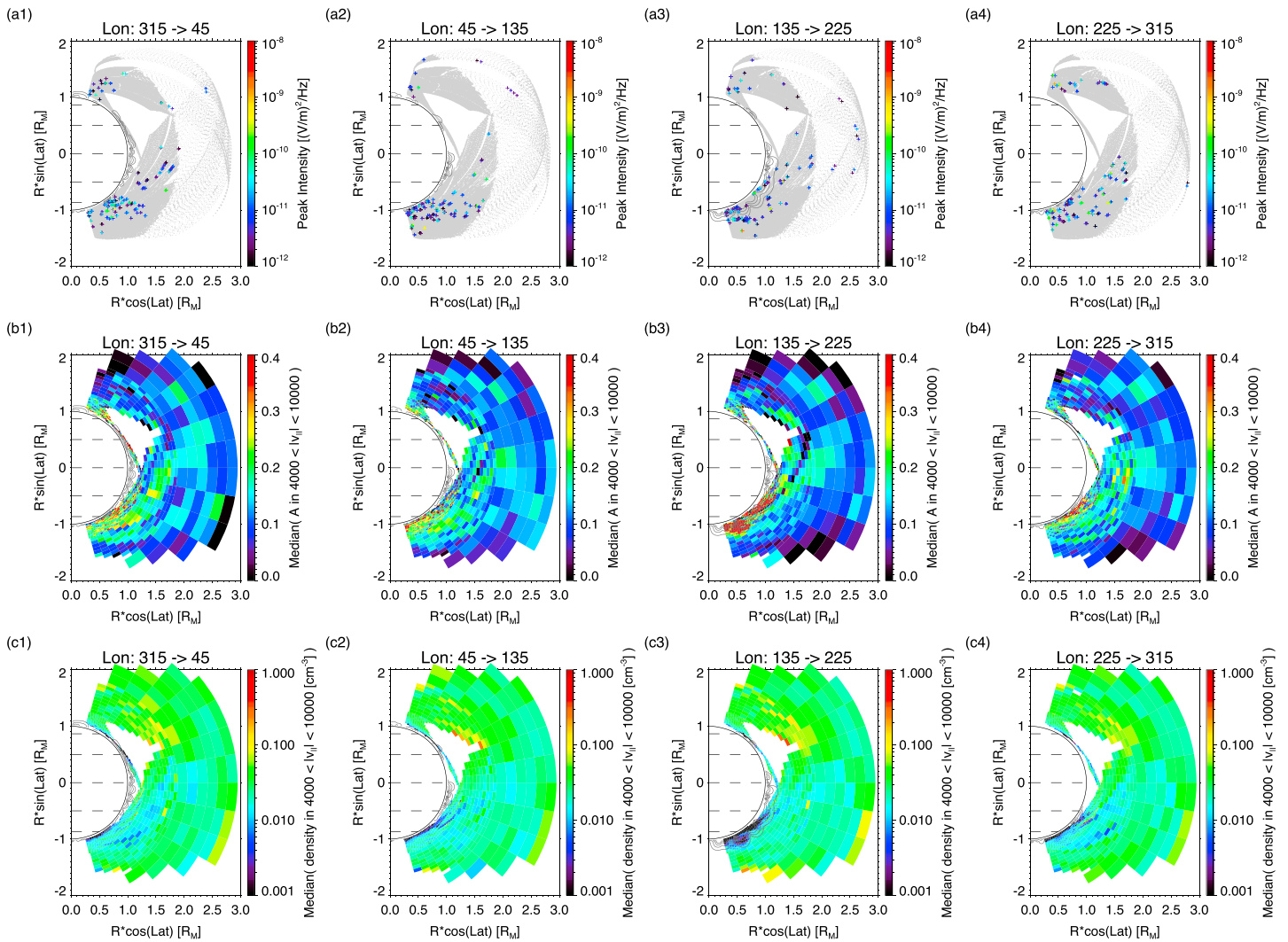


Figure 8. Longitudinal cuts of (a1–a4) geographic distributions of narrowband wave events, (b1–b4) medians of electron anisotropy, and (c1–c4) partial density in the 4000 km/s < $|v_{||}$ < 10,000 km/s range. The data used here are taken in the nightside magnetosphere at $X_{M50} < 0$ and below the nominal MPB. The gray contours show horizontal component strengths of crustal magnetic fields [Morschhauser et al., 2014] for 10, 20, 40, and 80 nT at the center longitudes.

Finally, we investigate geographic distributions of the narrowband wave events and anisotropic electrons and their association with crustal magnetic fields. As shown in Figure 7, both the narrowband wave occurrence and electron anisotropy vary as a function of altitude and solar zenith angle. Here we present altitude-latitude distributions of the nightside events ($X_{M50} < 0$) in comparison with magnetic field topology. Figure 8 shows $R \cos(\text{Latitude}) - R \sin(\text{Latitude})$ distributions of the narrowband wave events, electron anisotropy, and partial density of 4000 km/s < $|v_{||}$ < 10,000 km/s electrons in four longitude ranges centered at 0°E, 90°E, 180°E, and 270°E. The gray contours represent strengths of the horizontal component of the model crustal magnetic fields from Morschhauser et al. [2014] at the center longitudes as reference to approximate magnetic field topology in the longitude ranges. Overall, the narrowband wave events (Figures 8a1–8a4) coincide well with the enhanced electron anisotropy (Figures 8b1–8b4), except at low altitudes in the strongest horizontal field regions at ~180°E longitudes in the Southern Hemisphere (Figures 8a3 and 8b3). In this region deep in the closed fields, though the electron anisotropy is high (red in Figure 8b3), we note that the density of the hot electrons responsible for the wave generation is significantly suppressed (black to dark blue in Figure 8c3). We also note that all of the three distributions show noticeable north-south asymmetry. We will discuss these observations in the following section.

4. Discussion

We have presented three case studies showing that narrowband features at $f_{\text{LHR}} < f < f_{\text{ce}}$ in electric field wave spectra observed by MAVEN in the Martian magnetosphere are consistent with electromagnetic whistler mode waves generated by cyclotron resonance with anisotropic electrons that have one-sided or two-sided loss cones. This scenario is statistically supported by the consistent spatial distributions of the narrowband wave events and electron anisotropy enhancement. In this section, we discuss the detailed characteristics of the narrowband waves and anisotropic electrons, but first we comment on the dayside populations included in the statistical results.

The dayside narrowband wave events and anisotropic electrons are clustered near the nominal MPB (Figure 7). This suggests that these waves and anisotropic electrons are of and/or originate from the magnetosheath. The location of the MPB can vary depending on a variety of parameters such as the upstream solar wind and magnetic field conditions, season, and relative location of crustal magnetic fields [e.g., *Crider et al., 2002; Brain et al., 2005*]. Therefore, the data sets obtained just below the nominal MPB include a number of sheath intervals. Enhanced electric field wave activity, including peaked spectra below f_{ce} , is commonly observed in the Martian magnetosheath [*Grard et al., 1989, 1991*]. Hot electrons with $T_{e\perp} > T_{e\parallel}$ are also common in the Martian magnetosheath [e.g., *Skalsky et al., 1998*]. At Earth, intense bursts of electromagnetic whistler mode waves at ~ 100 Hz, known as “lion roars,” are observed in close association with mirror mode structures in the magnetosheath [e.g., *Smith and Tsurutani, 1976*] and in the magnetosphere close to the magnetopause [*Baumjohann et al., 2000; Dubinin et al., 2007*]. Proposed generation mechanisms for the lion roars involve cyclotron resonance with anisotropic electrons ($T_{e\perp} > T_{e\parallel}$) and enhancement of whistler mode growth by the decreased magnetic field strength and increased electron density in the mirror mode waves [*Thorne and Tsurutani, 1981*]. Detailed analysis of the properties and causal relationship of the dayside sheath electrons and waves at Mars is beyond the scope of the paper. Meanwhile, the nightside populations are not clustered near the nominal MPB but distributed deeper in the tail, implying that they are not sheath origin. Hereafter, we focus on these nightside magnetospheric waves and anisotropic electrons.

We observe the enhanced electron anisotropy on the nightside compared to the dayside (Figure 7c). Electron loss cones are not limited to the nightside but observed on the dayside as well [e.g., *Brain et al., 2007*]. However, the suprathermal tail populations of ionospheric photoelectrons, which fill parts of the loss cones, render the anisotropy smaller. The reduction of anisotropy on the dayside is consistent with the Mars Global Surveyor observations [*Brain et al., 2007*], which show that fully isotropic distributions (in the measured pitch angle ranges) are the most common type of pitch angle distributions on the dayside (at a fixed altitude and local time of 400 km and 2 P.M.) over a broad geographic region. Thus, the combination of the loss of ambient parallel electrons to the collisional atmosphere and little/no presence of ionospheric photoelectrons on the nightside field lines leads to the nightside anisotropy enhancement.

The altitude-latitude distributions of the narrowband wave events, electron anisotropy, and partial electron densities exhibit the clear north-south asymmetry (Figure 8). However, this does not necessarily reflect “true” geographic asymmetry because the orbital coverage of the data obtained in the Northern and Southern Hemispheres is heavily biased in MSO coordinates. Figure 9 shows median ρ_{MSO} in each altitude-latitude bin. It is seen that the measurements in the Southern Hemisphere were obtained mainly in the deep tail with small ρ_{MSO} , while the Northern Hemisphere data were taken at flanks with large ρ_{MSO} . A larger volume of data with better coverage both in MSO and geographic coordinates are required to unambiguously separate the MSO and geographic dependence.

The narrowband wave events are not observed at the low-altitude closed field regions (Figure 8a3) despite the large anisotropy (Figure 8b3). This is most likely due to the depleted suprathermal electron flux on the closed field lines (Figure 8c3) [*Mitchell et al., 2001; Brain et al., 2007; Steckiewicz et al., 2015*]. As seen at 05:58–06:00 UT in the third case study (Figure 4), the depleted hot electrons, though anisotropic, cannot provide sufficient free energy for rapid wave growth. In addition to the absence of narrowband wave events on low-altitude closed field lines, Figure 8a3 shows that the wave events are clustered in likely cusp regions between the two $|B_h|$ contour arcades as well as near the top of the $|B_h| = 10$ nT contour line. This suggests that the wave occurrence is controlled by the local magnetic field topology.

The LPW burst waveform data obtained on closed field lines reveal the frequency-time structures with time scales less than a second (Figure 6). The rising tones and two bands above and below half the electron

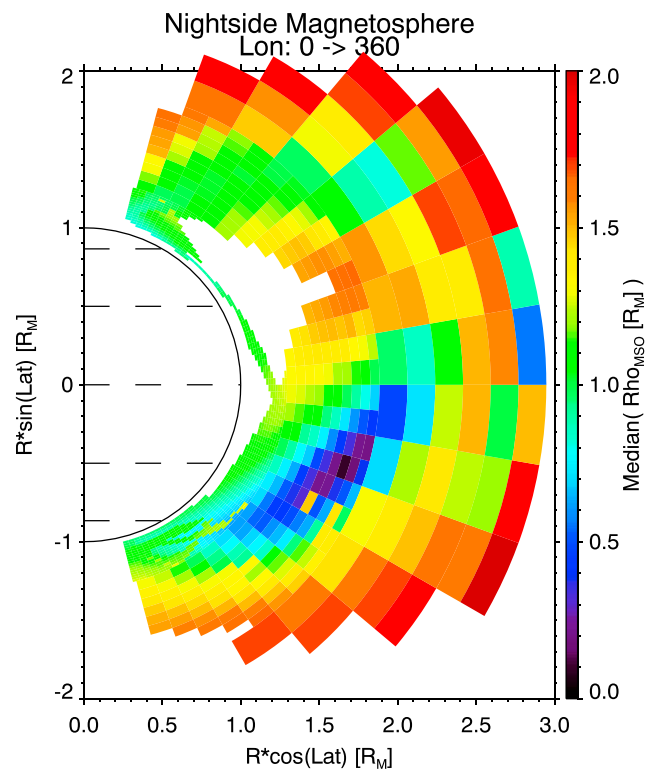


Figure 9. Altitude-latitude distribution of ρ_{MSO} for the data used in Figure 8.

cyclotron frequency resemble the characteristic signatures of the whistler mode chorus waves in the Earth's magnetosphere [Burtis and Helliwell, 1969, 1976; Tsurutani and Smith, 1974]. We note that though the linear theory successfully predicts the spectral peaks of the observed narrowband waves (Figures 2–5), nonlinear mechanisms could be implicated in the wave generation and growth processes. For example, Dubinin *et al.* [2007] demonstrated that bursty, coherent wave packets of whistler mode emissions can be explained by nonlinear whistler solitary waves. The discrete rising tones could be generated by a nonlinear growth mechanism [Omura *et al.*, 2008]. Future studies should investigate whether these spectral features at Mars are unique to closed field line configuration and identify their generation mechanisms. Also, the chorus waves in the Earth's magnetosphere play a significant role in pitch angle diffusion of plasma sheet electrons leading to diffuse auroral precipitation [e.g., Ni *et al.*, 2011]. Similar electron precipitation by wave-particle interaction may be possible for trapped electrons on closed field

lines at Mars, while only upward traveling loss cone electrons will be isotropized by downward propagating waves on open field lines. Evaluation of the wave-induced electron precipitation into the Martian atmosphere would be another important task if we are to fully address the electron dynamics and energetics in the Martian system.

5. Conclusions

MAVEN observations of electric and magnetic fields and electron velocity distributions have revealed that anisotropic electrons with one-sided or two-sided loss cones excite electromagnetic whistler mode waves with narrowband features between the electron cyclotron and lower hybrid frequencies in the nightside Martian magnetosphere. The narrowband waves are observed on both open and closed field lines and have spatial distributions similar to those of anisotropic electrons. The geographic distributions of the narrowband wave events and anisotropic electrons around the strongest crustal magnetic fields suggest that the local magnetic field topology controls both the anisotropy and abundance of hot electrons, thereby regulating the whistler mode wave generation. Analysis of the waveform data reveals that some of the narrowband waves on closed field lines contain complex frequency-time structures such as discrete elements of rising tones and two bands above and below half the electron cyclotron frequency. The whistler mode waves driven by anisotropic hot electrons, previously observed in intrinsic magnetospheres and at unmagnetized airless bodies, are now confirmed at Mars. The contribution of whistler mode wave-induced pitch angle scattering to electron precipitation into the Martian atmosphere should be evaluated in future studies.

References

Anderson, R. R., and K. Maeda (1977), VLF emissions associated with enhanced magnetospheric electrons, *J. Geophys. Res.*, *82*(1), 135–146, doi:10.1029/JA082i001p0135.

Andersson, L., R. E. Ergun, G. T. Delory, A. Eriksson, J. Westfall, H. Reed, J. McCauly, D. Summers, and D. Meyers (2015), The Langmuir Probe and Waves (LPW) instrument for MAVEN, *Space Sci. Rev.*, *195*(1), 173–198, doi:10.1007/s11214-015-0194-3.

Baumjohann, W., E. Georgescu, K.-H. Fornacon, H. U. Auster, R. A. Treumann, and G. Haerendel (2000), Magnetospheric lion roars, *Ann. Geophys.*, *18*(4), 406–410, doi:10.1007/s00585-000-0406-2.

Acknowledgments

The authors wish to acknowledge great support from the team members of the MAVEN mission. The research presented in this paper was funded by the NASA MAVEN Project and the French space agency CNES. G.A.D. was supported by a NASA Postdoctoral Program appointment at the NASA Goddard Space Flight Center, administered by Universities Space Research Association through a contract with NASA. MAVEN data are publicly available through the Planetary Data System (<http://ppi.pds.nasa.gov/mission/MAVEN>).

- Brain, D. A., F. Bagenal, M. H. Acuña, J. E. P. Connerney, D. H. Crider, C. Mazelle, D. L. Mitchell, and N. F. Ness (2002), Observations of low-frequency electromagnetic plasma waves upstream from the Martian shock, *J. Geophys. Res.*, *107*(A6), 1076, doi:10.1029/2000JA000416.
- Brain, D. A., J. S. Halekas, R. Lillis, D. L. Mitchell, R. P. Lin, and D. H. Crider (2005), Variability of the altitude of the Martian sheath, *Geophys. Res. Lett.*, *32*, L18203, doi:10.1029/2005GL023126.
- Brain, D. A., R. J. Lillis, D. L. Mitchell, J. S. Halekas, and R. P. Lin (2007), Electron pitch angle distributions as indicators of magnetic field topology near Mars, *J. Geophys. Res.*, *112*, A09201, doi:10.1029/2007JA012435.
- Burtis, W., and R. Helliwell (1976), Magnetospheric chorus: Occurrence patterns and normalized frequency, *Planet. Space Sci.*, *24*(11), 1007–1024, doi:10.1016/0032-0633(76)90119-7.
- Burtis, W. J., and R. A. Helliwell (1969), Banded chorus—A new type of VLF radiation observed in the magnetosphere by OGO 1 and OGO 3, *J. Geophys. Res.*, *74*(11), 3002–3010, doi:10.1029/JA074i011p03002.
- Connerney, J., J. Espley, P. Lawton, S. Murphy, J. Odum, R. Oliverson, and D. Sheppard (2015), The MAVEN magnetic field investigation, *Space Sci. Rev.*, *195*, 257–291, doi:10.1007/s11214-015-0169-4.
- Crider, D. H., et al. (2002), Observations of the latitude dependence of the location of the Martian magnetic pileup boundary, *Geophys. Res. Lett.*, *29*(8), 1170, doi:10.1029/2001GL013860.
- Delva, M., and E. Dubinin (1998), Upstream ULF fluctuations near Mars, *J. Geophys. Res.*, *103*(A1), 317–326, doi:10.1029/97JA02501.
- DiBraccio, G. A., et al. (2015), Magnetotail dynamics at Mars: Initial MAVEN observations, *Geophys. Res. Lett.*, *42*, 8828–8837, doi:10.1002/2015GL065248.
- Dubinin, E., and M. Fraenz (2016), *Ultra-Low-Frequency Waves at Venus and Mars*, chap. 20, pp. 343–364, John Wiley, Hoboken, N. J., doi:10.1002/9781119055006.ch20.
- Dubinin, E., M. Fraenz, A. Fedorov, R. Lundin, N. Edberg, F. Duru, and O. Vaisberg (2012), Ion energization and escape on Mars and Venus, *Space Sci. Rev.*, *162*, 173–211, doi:10.1007/978-1-4614-3290-6_6.
- Dubinin, E. M., et al. (2007), Coherent whistler emissions in the magnetosphere—Cluster observations, *Ann. Geophys.*, *25*(1), 303–315, doi:10.5194/angeo-25-303-2007.
- Ergun, R. E., L. Andersson, W. K. Peterson, D. Brain, G. T. Delory, D. L. Mitchell, R. P. Lin, and A. W. Yau (2006), Role of plasma waves in Mars' atmospheric loss, *Geophys. Res. Lett.*, *33*, L14103, doi:10.1029/2006GL025785.
- Espley, J. R., P. A. Cloutier, D. A. Brain, D. H. Crider, and M. H. Acuña (2004), Observations of low-frequency magnetic oscillations in the Martian magnetosheath, magnetic pileup region, and tail, *J. Geophys. Res.*, *109*, A07213, doi:10.1029/2003JA010193.
- Gosling, J. T., R. M. Skoug, D. J. McComas, and C. W. Smith (2005), Direct evidence for magnetic reconnection in the solar wind near 1 au, *J. Geophys. Res.*, *110*, A01107, doi:10.1029/2004JA010809.
- Grard, R., C. Nairn, A. Pedersen, S. Klimov, S. Savin, A. Skalsky, and J. Trotignon (1991), Plasma and waves around Mars, *Planet. Space Sci.*, *39*(1), 89–98, doi:10.1016/0032-0633(91)90131-S.
- Grard, R., A. Pedersen, S. Klimov, S. Savin, A. Skalsky, J. G. Trotignon, and C. Kennel (1989), First measurements of plasma waves near Mars, *Nature*, *341*(6243), 607–609, doi:10.1038/341607a0.
- Gurnett, D., D. Morgan, F. Duru, F. Akalin, J. Winningham, R. Frahm, E. Dubinin, and S. Barabash (2010), Large density fluctuations in the Martian ionosphere as observed by the Mars Express radar sounder, *Icarus*, *206*(1), 83–94, doi:10.1016/j.icarus.2009.02.019, solar Wind Interactions with Mars.
- Halekas, J. S., D. A. Brain, and J. P. Eastwood (2011), Large-amplitude compressive “sawtooth” magnetic field oscillations in the Martian magnetosphere, *J. Geophys. Res.*, *116*, A07222, doi:10.1029/2011JA016590.
- Halekas, J. S., et al. (2012), Lunar precursor effects in the solar wind and terrestrial magnetosphere, *J. Geophys. Res.*, *117*, A05101, doi:10.1029/2011JA017289.
- Halekas, J. S., et al. (2015), Time-dispersed ion signatures observed in the Martian magnetosphere by MAVEN, *Geophys. Res. Lett.*, *42*, 8910–8916, doi:10.1002/2015GL064781.
- Harada, Y., and J. S. Halekas (2016), Upstream waves and particles at the Moon, in *Low-Frequency Waves in Space Plasmas*, edited by A. Keiling, D.-H. Lee, and V. Nakariakov, pp. 307–322, John Wiley, Hoboken, N. J., doi:10.1002/9781119055006.ch18.
- Harada, Y., J. S. Halekas, A. R. Poppe, S. Kurita, and J. P. McFadden (2014), Extended lunar precursor regions: Electron-wave interaction, *J. Geophys. Res. Space Physics*, *119*, 9160–9173, doi:10.1002/2014JA020618.
- Harada, Y., et al. (2015a), Magnetic reconnection in the near-Mars magnetotail: MAVEN observations, *Geophys. Res. Lett.*, *42*, 8838–8845, doi:10.1002/2015GL065004.
- Harada, Y., J. S. Halekas, A. R. Poppe, Y. Tsugawa, S. Kurita, and J. P. McFadden (2015b), Statistical characterization of the forenoon particle and wave morphology: ARTEMIS observations, *J. Geophys. Res. Space Physics*, *120*, 4907–4921, doi:10.1002/2015JA021211.
- Harada, Y., et al. (2016), MAVEN observations of energy-time dispersed electron signatures in Martian crustal magnetic fields, *Geophys. Res. Lett.*, *43*, 939–944, doi:10.1002/2015GL067040.
- Horne, R. B., and R. M. Thorne (2003), Relativistic electron acceleration and precipitation during resonant interactions with whistler-mode chorus, *Geophys. Res. Lett.*, *30*(10), 1527, doi:10.1029/2003GL016973.
- Horne, R. B., R. M. Thorne, N. P. Meredith, and R. R. Anderson (2003), Diffuse auroral electron scattering by electron cyclotron harmonic and whistler mode waves during an isolated substorm, *J. Geophys. Res.*, *108*(A7), 1290, doi:10.1029/2002JA009736.
- Jakosky, B. M., et al. (2015), The Mars Atmosphere and Volatile Evolution (MAVEN) mission, *Space Sci. Rev.*, *195*, 3–48, doi:10.1007/s11214-015-0139-x.
- Kennel, C. F., and H. E. Petschek (1966), Limit on stably trapped particle fluxes, *J. Geophys. Res.*, *71*, 1–28, doi:10.1029/JZ071i001p00001.
- Li, W., R. M. Thorne, N. P. Meredith, R. B. Horne, J. Bortnik, Y. Y. Shprits, and B. Ni (2008), Evaluation of whistler mode chorus amplification during an injection event observed on CRRES, *J. Geophys. Res.*, *113*, A09210, doi:10.1029/2008JA013129.
- Li, W., et al. (2013), An unusual enhancement of low-frequency plasmaspheric hiss in the outer plasmasphere associated with substorm-injected electrons, *Geophys. Res. Lett.*, *40*, 3798–3803, doi:10.1002/grl.50787.
- Lillis, R. J., D. L. Mitchell, R. P. Lin, and M. H. Acuña (2008), Electron reflectometry in the Martian atmosphere, *Icarus*, *194*(2), 544–561, doi:10.1016/j.icarus.2007.09.030.
- Lundin, R. (2011), Ion acceleration and outflow from Mars and Venus: An overview, *Space Sci. Rev.*, *162*(1–4), 309–334, doi:10.1007/s11214-011-9811-y.
- Lundin, R., S. Barabash, E. Dubinin, D. Winningham, and M. Yamauchi (2011), Low-altitude acceleration of ionospheric ions at Mars, *Geophys. Res. Lett.*, *38*, L08108, doi:10.1029/2011GL047064.
- Mazelle, C., et al. (2004), Bow shock and upstream phenomena at Mars, *Space Sci. Rev.*, *111*(1–2), 115–181, doi:10.1023/B:SPAC.0000032717.98679.d0.

- McFadden, J. P., et al. (2015), MAVEN SupraThermal and Thermal Ion Composition (STATIC) instrument, *Space Sci. Rev.*, *195*(1–4), 199–256, doi:10.1007/s11214-015-0175-6.
- Means, J. D. (1972), Use of the three-dimensional covariance matrix in analyzing the polarization properties of plane waves, *J. Geophys. Res.*, *77*(28), 5551–5559, doi:10.1029/JA077i028p05551.
- Menietti, J. D., Y. Y. Shprits, R. B. Horne, E. E. Woodfield, G. B. Hospodarsky, and D. A. Gurnett (2012), Chorus, ECH, and Z mode emissions observed at Jupiter and Saturn and possible electron acceleration, *J. Geophys. Res.*, *117*, A12214, doi:10.1029/2012JA018187.
- Mitchell, D., R. Lin, C. Mazelle, H. Reme, P. Cloutier, J. Connerney, M. Acuña, and N. Ness (2001), Probing Mars' crustal magnetic field and ionosphere with the MGS electron reflectometer, *J. Geophys. Res.*, *106*(E10), 23,419–23,427, doi:10.1029/2000JE001435.
- Mitchell, D. L., et al. (2016), The MAVEN solar wind electron analyzer, *Space Sci. Rev.*, *200*, 495–528, doi:10.1007/s11214-015-0232-1.
- Morschhauser, A., V. Lesur, and M. Grott (2014), A spherical harmonic model of the lithospheric magnetic field of Mars, *J. Geophys. Res. Planets*, *119*, 1162–1188, doi:10.1002/2013JE004555.
- Nagy, A., et al. (2004), The plasma environment of Mars, *Space Sci. Rev.*, *111*(1–2), 33–114, doi:10.1023/B:SPAC.0000032718.47512.92.
- Ni, B., R. M. Thorne, N. P. Meredith, R. B. Horne, and Y. Y. Shprits (2011), Resonant scattering of plasma sheet electrons leading to diffuse auroral precipitation: 2. Evaluation for whistler mode chorus waves, *J. Geophys. Res.*, *116*, A04219, doi:10.1029/2010JA016233.
- Omura, Y., Y. Katoh, and D. Summers (2008), Theory and simulation of the generation of whistler-mode chorus, *J. Geophys. Res.*, *113*, A04223, doi:10.1029/2007JA012622.
- Romanelli, N., C. Bertucci, D. Gómez, C. Mazelle, and M. Delva (2013), Proton cyclotron waves upstream from Mars: Observations from Mars Global Surveyor, *Planet. Space Sci.*, *76*, 1–9, doi:10.1016/j.pss.2012.10.011.
- Ruhunusiri, S., J. S. Halekas, J. E. P. Connerney, J. R. Spley, J. P. McFadden, D. E. Larson, D. L. Mitchell, C. Mazelle, and B. M. Jakosky (2015), Low frequency waves in the Martian magnetosphere and their response to upstream solar wind driving conditions, *Geophys. Res. Lett.*, *42*, 8917–8924, doi:10.1002/2015GL064968.
- Ruhunusiri, S., et al. (2016a), MAVEN observation of an obliquely propagating low-frequency wave upstream of Mars, *J. Geophys. Res. Space Physics*, *121*, 2374–2389, doi:10.1002/2015JA022306.
- Ruhunusiri, S., et al. (2016b), MAVEN observations of partially developed Kelvin-Helmholtz vortices at Mars, *Geophys. Res. Lett.*, *43*, 4763–4773, doi:10.1002/2016GL068926.
- Russell, C. T. (1991), Venus lightning, *Space Sci. Rev.*, *55*(1), 317–356, doi:10.1007/BF00177140.
- Russell, C. T., J. G. Luhmann, K. Schwingenschuh, W. Riedler, and Y. Yeroshenko (1990), Upstream waves at Mars: Phobos observations, *Geophys. Res. Lett.*, *17*(6), 897–900, doi:10.1029/GL017i006p00897.
- Russell, C. T., T. L. Zhang, M. Delva, W. Magnes, R. J. Strangeway, and H. Y. Wei (2007), Lightning on Venus inferred from whistler-mode waves in the ionosphere, *Nature*, *450*(7170), 661–662, doi:10.1038/nature05930.
- Russell, C. T., T. L. Zhang, and H. Y. Wei (2008), Whistler mode waves from lightning on Venus: Magnetic control of ionospheric access, *J. Geophys. Res.*, *113*, E00B05, doi:10.1029/2008JE003137.
- Santolik, O., D. A. Gurnett, G. H. Jones, P. Schippers, F. J. Cray, J. S. Leisner, G. B. Hospodarsky, W. S. Kurth, C. T. Russell, and M. K. Dougherty (2011), Intense plasma wave emissions associated with Saturn's moon Rhea, *Geophys. Res. Lett.*, *38*, L19204, doi:10.1029/2011GL049219.
- Skalsky, A., E. M. Dubinin, A. Petrukovich, K. Sauer, P. Kiraly, and K. Schwingenschuh (1998), Ion and electron heating at the Martian bow shock. Common for bow shocks or not?, *Earth Planets Space*, *50*(3), 289–294, doi:10.1186/BF03352115.
- Smith, E. J., and B. T. Tsurutani (1976), Magnetosheath lion roars, *J. Geophys. Res.*, *81*(13), 2261–2266, doi:10.1029/JA081i013p02261.
- Steckiewicz, M., et al. (2015), Altitude dependence of nightside Martian suprathermal electron depletions as revealed by MAVEN observations, *Geophys. Res. Lett.*, *42*, 8877–8884, doi:10.1002/2015GL065257.
- Summers, D., R. Tang, and R. M. Thorne (2009), Limit on stably trapped particle fluxes in planetary magnetospheres, *J. Geophys. Res.*, *114*, A10210, doi:10.1029/2009JA014428.
- Thorne, R., and B. Tsurutani (1981), The generation mechanism for magnetosheath lion roars, *Nature*, *293*(5831), 384–386, doi:10.1038/293384a0.
- Trotignon, J., A. Trotignon, E. Dubinin, A. Skalsky, R. Grard, and K. Schwingenschuh (2000), Planetary ionospheres and magnetospheres electron plasma waves beyond the Mars' bow shock: The PWS/Phobos-2 observations, *Adv. Space Res.*, *26*(10), 1619–1622, doi:10.1016/S0273-1177(00)00106-X.
- Trotignon, J., C. Mazelle, C. Bertucci, and M. Acuña (2006), Martian shock and magnetic pile-up boundary positions and shapes determined from the phobos 2 and Mars global surveyor data sets, *Planet. Space Sci.*, *54*(4), 357–369, doi:10.1016/j.pss.2006.01.003.
- Trotignon, J. G., R. Grard, and S. Savin (1991), Plasma wave system measurements of the Martian bow shock from the Phobos 2 spacecraft, *J. Geophys. Res.*, *96*(A7), 11,253–11,264, doi:10.1029/91JA00502.
- Tsurutani, B. T., and E. J. Smith (1974), Postmidnight chorus: A substorm phenomenon, *J. Geophys. Res.*, *79*(1), 118–127, doi:10.1029/JA079i001p00118.
- Wei, H. Y., and C. T. Russell (2006), Proton cyclotron waves at Mars: Exosphere structure and evidence for a fast neutral disk, *Geophys. Res. Lett.*, *33*, L23103, doi:10.1029/2006GL026244.